Experimentally Validated Simulator of Flight Dynamics: for a Magnus Effect-based Quadcopter System

Zakeye Azaki, Pierre Susbielle, Alexis Offermann, Jonathan Dumon, Nacim Meslem, Ahmad Hably, Amaury Nègre

Experimentally Validated Simulator of Flight Dynamics: for a Magnus Effect-based Quadcopter System

Zakeye AZAKI*, Pierre SUSBIELLE, Alexis OFFERMANN, Jonathan DUMON,
Nacim MESLEM, Ahmad HABLY, Amaury NEGRE
Univ. Grenoble Alpes, CNRS, Grenoble-INP, GIPSA-lab, F-38000, Grenoble, France

ABSTRACT

Unmanned aerial vehicles (UAVs) have gained extensive utilization across diverse industries, necessitating enhancing their capabilities through addressing their power consumption limitations. In this context, the Magnus effect can increase UAV autonomy by exploiting its aerodynamic capabilities. The presented study contributes a reliable 6-DoF nonlinear simulator tailored for a drone equipped with Magnus cylinders system. Through the execution of experimental flights, the simulator's performance is rigorously validated, establishing its reliability for future deployments.

keywords: Flight Dynamics Simulator, Flight Dynamics Modeling, Experimental Validations, Quadcopters, Magnus Effect.

1 INTRODUCTION

In recent years, unmanned aerial vehicles (UAVs) have become increasingly prevalent across various industries and applications. One can cite industrial surveillance [1], infrastructure inspections [2], cinematography [3], merchandise transport [4] or aerial manipulation [5]. Developing UAVs that can fly longer distances and perform more complex tasks is an ongoing challenge, and their power consumption is one of the main factors affecting their range and endurance. Researchers have been exploring various methods for reducing UAVs' energy consumption to address this issue. In recent years, there has been renewed interest in the Magnus effect, which has been known for over a century [6], but has gained renewed attention in light of its potential application to UAVs [7, 8]. With Magnus cylinders attached to UAVs, lift can be generated without traditional flight controls such as flaps or rudders, and flight trajectory can be controlled more precisely and flexibly.

Magnus cylinders offer several advantages over traditional control surfaces. These include that the speed and direction of rotation of the cylinders may be controlled robustly to create the desired aerodynamic forces, thereby providing greater control over the flight path of an aircraft. The Magnus effect can also reduce the power consumption as it generates lift, which helps maintain altitude, reducing the amount of power required to maintain the UAV's altitude. This is particularly relevant for UAVs that fly long distances over extended periods, such as those used in search and rescue missions etc. The Magnus effect can improve UAV technology by providing enhanced control and reducing energy consumption.

In this context, the presented study aims to develop a reliable 6-DoF nonlinear simulator for the quadcopter with the Magnus cylinder system. This will provide a comprehensive description of the system and help in the design of future autopilots in the applications of airborne wind energy production [9, 10].

PaperOrganisation **:** Firstly, Section 2 addresses the flight mechanics model of the Magnus-based quadcopter. It begins by presenting the equations of motion, covering both translational and rotational dynamics. In Section 3, a detailed explanation of all the forces and torques acting on the system is provided. The design of the PID-based position control strategy is explained in Section 4. Moving on, Section 5 provides a brief description of the experimental setup used for validating the simulator. Finally, Section 6 presents an overview of the overall simulator along with the reliability study and simulator validation by analyzing and comparing some simulations and experimental flight results.

Notations **:** For seeking clarity, a series of notations is defined. For vector $\boldsymbol{x}$, we denote by $||\boldsymbol{x}||$ the $\mathcal{L}_2$ norm of $\boldsymbol{x}$ and by $\overline{\boldsymbol{x}}$ its transpose. $[\boldsymbol{x}]^{\mathcal{A}}$ is the representation of $\boldsymbol{x}$ expressed in $\mathcal{A}$ coordinate frame and $D^{\mathcal{A}}\boldsymbol{x}$ its derivative w.r.t frame $\mathcal{A}$. Regarding the dynamics, $\boldsymbol{s}_{BA}$ denotes the displacement vector of point B w.r.t point A, on the other hand, $\boldsymbol{S}_{BA}$ represents the skew matrix of the position vector $\boldsymbol{s}_{BA}$. Vector $\boldsymbol{v}_B^{\mathcal{A}}$ represents the linear velocity of point mass B w.r.t $\mathcal{A}$ coordinate frame and $\boldsymbol{w}^{\mathcal{B}\mathcal{A}}$ is the angular velocity vector of frame $\mathcal{B}$ w.r.t frame $\mathcal{A}$. Given an angle θ we denote c_θ, s_θ, and t_θ to the cosine, sin, and tangent of θ.

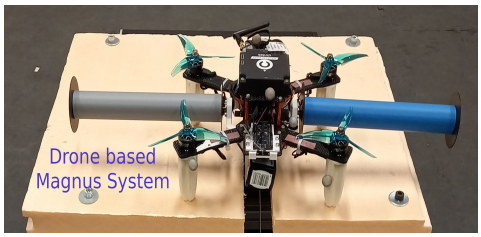

Figure 1: Magnus Effect-based Quadcopter prototype.

*Email address: zakeye.azaki@gipsa-lab.grenoble-inp.fr

2 NONLINEAR FLIGHT MECHANICS MODEL

The Magnus-based quadcopter system consists of a quadrotor drone and two spinning Magnus cylinders connected to the right and left of the drone, respectively, as shown in Figure 1. Table 1 represents the involved parameters of the system. The standard flight mechanics theory [11] is used to derive the 6-DoF nonlinear dynamics that govern the system's behavior. All the following parameters and equations are used and coded in MATLAB/Simulink to form the core of the realistic Magnus Effect-based Quadcopter System Simulator. The following reference frames are defined to formulate the equations of motion,

- Inertial Frame $\mathcal{I}(\boldsymbol{i}_1, \boldsymbol{i}_2, \boldsymbol{i}_2)$: Its base point I is assumed to be the reference of the position measurements.
- Drone Body Frame $\mathcal{D}'(\boldsymbol{d}_1, \boldsymbol{d}_2, \boldsymbol{d}_3)$: Its base point coincides with the drone's center of mass D. The base vectors $\boldsymbol{d}_1$, $\boldsymbol{d}_2$, and $\boldsymbol{d}_3$ are aligned with the principle axes of the moment of inertia, such that $\boldsymbol{d}_3$ is directed upwards.
- Right Magnus Frame $\mathcal{M}_r(\boldsymbol{m}_{r_1}, \boldsymbol{m}_{r_2}, \boldsymbol{m}_{r_3})$: Its base point coincides with the right Magnus wing center of mass M_r. The base vector $\boldsymbol{m}_{r_2}$ is aligned with the right Magnus cylinder axis of rotations.
- Left Magnus Frame $\mathcal{M}_l(\boldsymbol{m}_{l_1}, \boldsymbol{m}_{l_2}, \boldsymbol{m}_{l_3})$: Its base point coincides with the left Magnus wing center of mass M_l. The base vector $\boldsymbol{m}_{l_2}$ is aligned with the left Magnus cylinder axis of rotations.
- System Body Frame $\mathcal{D}(\boldsymbol{d}_1, \boldsymbol{d}_2, \boldsymbol{d}_3)$: Its base point coincides with the system drone+Magnus's center of mass C. The base vectors are parallel to that of $\mathcal{D}'$. This frame is considered the body frame supporting all other spinning bodies.

The rotation matrix in this flight mechanics $\boldsymbol{R}^{\mathcal{DI}}$ is the one of system frame $\mathcal{D}$ w.r.t inertial frame $\mathcal{I}$. It comprises three rotations by the so-called Euler angles: roll, pitch, yaw or ϕ, θ, and ψ. In our simulator, we use quaternions instead of Euler angles to represent the drone's rotation, as quaternions avoid the problem of gimbal lock and are more computationally efficient. The rotation quaternion is represented by the four-dimensional coordinates $\overline{\boldsymbol{q}} = \begin{bmatrix} q_0 & q_1 & q_2 & q_3 \end{bmatrix}$.

Parameter	Description	Value
m	Total mass	1.568 kg
m_D	Drone mass	1.47 kg
m_{M_k}	kth Magnus mass	0.049 kg
L_{M_k}	kth Magnus length	0.179 m
R_{M_k}	kth Magnus radius	0.0175 m

Table 1: Model Parameters

It is assumed that the two-unit directions $\boldsymbol{m}_{r_2}$ and $\boldsymbol{m}_{l_2}$ are collinear and they are parallel to $\boldsymbol{d}_2$ with an offset along $\boldsymbol{d}_3$ of δ_z such that,

$$[\overline{\boldsymbol{s}_{M_r D}}]^{\mathcal{D}} = \begin{bmatrix} 0 & \frac{L_r}{2} & -\delta_z \end{bmatrix} \ , \ [\overline{\boldsymbol{s}_{M_l D}}]^{\mathcal{D}} = \begin{bmatrix} 0 & \frac{-L_l}{2} & -\delta_z \end{bmatrix} \tag{2.1}$$

The common center of mass C can be determined as follows,

$$[\boldsymbol{s}_{CD}]^{\mathcal{D}} = \frac{\sum_k m_{M_k} [\boldsymbol{s}_{M_k D}]^{\mathcal{D}}}{m} \tag{2.2}$$

2.1 System Mathematical Model

First, it is important to mention that the centers of mass are mutually fixed. The translational and attitude dynamic equations are formulated using Newton's and Euler's laws of clustered bodies, respectively:

$$m D^{\mathcal{I}} \boldsymbol{v}_C^{\mathcal{I}} = \boldsymbol{F}_C + \boldsymbol{F}_D + \sum_k \boldsymbol{F}_{M_k} + \boldsymbol{P} \tag{2.3}$$

$$D^{\mathcal{I}}(\boldsymbol{I}_D^{\mathcal{D}} \boldsymbol{w}^{\mathcal{DI}}) + D^{\mathcal{I}}(m_D \overline{\boldsymbol{S}}_{DC} \boldsymbol{S}_{DC} \boldsymbol{w}^{\mathcal{DI}}) + \sum_k D^{\mathcal{I}}(\boldsymbol{I}_{M_k}^{\mathcal{M}_k} \boldsymbol{w}^{\mathcal{M}_k \mathcal{I}}) + \sum_k D^{\mathcal{I}}(m_{M_k} \overline{\boldsymbol{S}}_{M_k C} \boldsymbol{S}_{M_k C} \boldsymbol{w}^{\mathcal{M}_k \mathcal{I}}) = \boldsymbol{\Gamma}_C + \boldsymbol{\Gamma}_D + \sum_k \boldsymbol{\Gamma}_{M_k} \tag{2.4}$$

where $k \in \{r, l\}$ represents the dynamics of the right and left Magnus separately and $\boldsymbol{P} = m\boldsymbol{g}$ is the system weight. The force vectors $\boldsymbol{F}_D$ and $\boldsymbol{F}_{M_k}$ are the total forces exerted on the system due to the drone propellers and Magnus cylinders, respectively. Similarly, $\boldsymbol{\Gamma}_D$ and $\boldsymbol{\Gamma}_{M_k}$ are the torques acting on the system due to the drone propellers and Magnus cylinders, respectively. However, the force vector $\boldsymbol{F}_C$ and the torque vector $\boldsymbol{\Gamma}_C$ are the additional control contributions. The detailed derivation of these forces and torques will be represented in the next sections.
The angular velocity dynamics can be derived from (2.4) by

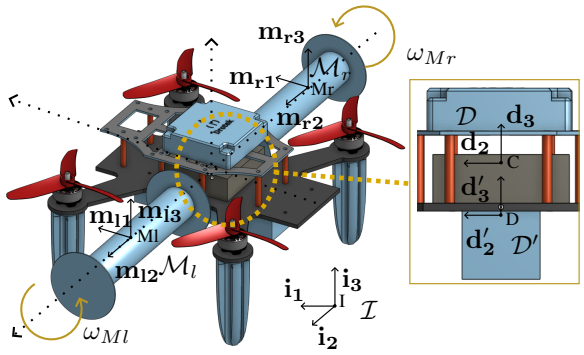

Figure 2: Frame definition on the quadcopter. From figure, $\mathcal{D}$ represents the body frame, $\mathcal{D}'$ the drone body frame, $\mathcal{M}_l$ the left Magnus frame, $\mathcal{M}_r$ the right Magnus frame and eventually $\mathcal{I}$ the inertial frame.

transferring the rotational derivative to the frame of the main body $\mathcal{D}$. We can deduce,

$$\begin{aligned} \boldsymbol{J}D^{\mathcal{D}}\boldsymbol{w}^{\mathcal{DI}} &= -\boldsymbol{\Omega}^{\mathcal{DI}}\boldsymbol{J}\boldsymbol{w}^{\mathcal{DI}} + \boldsymbol{\Gamma}_C + \boldsymbol{\Gamma}_D + \sum_k \boldsymbol{\Gamma}_{M_k} \\ &- \sum_k (\boldsymbol{\Omega}^{\mathcal{DI}}\boldsymbol{I}_{M_k}^{\mathcal{M}_k}\boldsymbol{w}^{\mathcal{M}_k\mathcal{D}}) - \sum_k (\boldsymbol{I}_{M_k}^{\mathcal{M}_k} D^{\mathcal{D}}\boldsymbol{w}^{\mathcal{M}_k\mathcal{D}}) \end{aligned} \tag{2.5}$$

such that:

$$\begin{cases} \boldsymbol{J}_D^{\mathcal{D}} = \boldsymbol{I}_D^{\mathcal{D}'} + m_D\overline{\boldsymbol{S}}_{DC}\boldsymbol{S}_{DC} \\ \boldsymbol{J}_M^{\mathcal{D}} = \sum_k (\boldsymbol{I}_{M_K}^{\mathcal{M}_K} + m_{M_k}\overline{\boldsymbol{S}}_{M_kC}\boldsymbol{S}_{M_kC}), \\ \boldsymbol{J} = \boldsymbol{J}_D^{\mathcal{D}} + \boldsymbol{J}_M^{\mathcal{D}} \end{cases} \tag{2.6}$$

The revolving angular velocity vectors and the moment of inertia matrix of each Magnus cylinder about its axis of symmetry are expressed as,

$$[\boldsymbol{w}^{\mathcal{M}_k\mathcal{D}}]^{\mathcal{D}} = \begin{bmatrix} 0 \\ w_{M_k} \\ 0 \end{bmatrix}, [\boldsymbol{I}_{M_k}^{\mathcal{M}_k}]^{\mathcal{D}} = \begin{bmatrix} IX_k & 0 & 0 \\ 0 & IY_k & 0 \\ 0 & 0 & IX_k \end{bmatrix} \tag{2.7}$$

As a result, the translational and attitude dynamic state variables correspond to frame $\mathcal{D}$'s linear and angular velocities w.r.t. frame $\mathcal{I}$, respectively:

$$[\boldsymbol{v}_C^{\mathcal{I}}]^{\mathcal{I}} = [\dot{\boldsymbol{s}}_{CI}]^{\mathcal{I}} = \begin{bmatrix} \dot{x} \\ y \\ z \end{bmatrix} \quad , \quad [\boldsymbol{w}^{\mathcal{DI}}]^{\mathcal{D}} = \begin{bmatrix} p \\ q \\ r \end{bmatrix} \tag{2.8}$$

Moreover, the skew matrix of the angular velocity vector $\boldsymbol{w}^{\mathcal{DI}}$ and the drone moment of inertia are expressed as:

$$\begin{aligned} [\boldsymbol{\Omega}^{\mathcal{DI}}]^{\mathcal{D}} &= \begin{bmatrix} 0 & -r & q \\ r & 0 & -p \\ -q & p & 0 \end{bmatrix}, \\ [\boldsymbol{I}_D^{\mathcal{D}'}]^{\mathcal{D}} &= \begin{bmatrix} IX & IXY & IXZ \\ IXY & IY & IYZ \\ IXZ & IYZ & IZ \end{bmatrix} \end{aligned} \tag{2.9}$$

The equation of angular position can be expressed in terms of angular velocities $\boldsymbol{w}^{\mathcal{DI}}$ expressed in $\mathcal{D}$. Based on the Euler ZYX formalism,

$$\begin{cases} \dot{\boldsymbol{\Theta}} = \begin{bmatrix} \dot{\phi} \\ \theta \\ \psi \end{bmatrix} &= \boldsymbol{W}^{-1}\boldsymbol{w}^{\mathcal{DI}} \\ \boldsymbol{W}^{-1} &= \begin{bmatrix} 1 & s_\phi t_\theta & c_\phi t_\theta \\ 0 & c_\phi & -s_\phi \\ 0 & s_\phi/c_\theta & c_\phi/c_\theta \end{bmatrix} \end{cases} \tag{2.10}$$

with $\boldsymbol{W}$ known as the Wronskien matrix of the Euler angles $\boldsymbol{\Theta}$ attitude representation. The quaternion formalism of the angles' dynamics is obtained as follows,

$$\dot{\boldsymbol{q}} = \frac{1}{2}\begin{bmatrix} 0 & -\overline{\boldsymbol{w}^{\mathcal{DI}}} \\ \boldsymbol{w}^{\mathcal{DI}} & \boldsymbol{\Omega}^{\mathcal{DI}} \end{bmatrix}\boldsymbol{q} \tag{2.11}$$

3 FORCES AND TORQUES

3.1 Actuator dynamics

The presented system uses six brushless motors as actuators. Each one of which is modeled in this work by its single-phase electromechanical equivalent model, defined as follows for w the motor rotation speed :

$$\begin{cases} J_r\dot{\omega} &= \Gamma_{mot} - \Gamma_{res} \\ U &= \text{sat}(e + RI + L\dot{I}) \end{cases} \tag{3.1}$$

Where J_r represents the inertia of the motor and load (Magnus or propeller) assembly, U, e, and I refer to the motor phase voltage, the electromechanical force, and the phase current. The phase resistance R and inductance L are directly measured on the motor. Motor torque Γ_{mot} is proportional to the phase current by electric constant K_c. Electromechanical force is proportional to the rotation speed through mechanical constant K_m. Resistive torque Γ_{res} can be approximated as the sum of an air friction quadratic torque, with C_Q the drag coefficient of the motor load, and a mechanical dry friction $\alpha\omega$:

$$\begin{cases} \Gamma_{mot} &= K_c I \\ \Gamma_{res} &= C_Q\omega^2 + \alpha\omega \\ e &= K_m\omega \end{cases} \tag{3.2}$$

In the rest of this paper, ω_{R_i} will refer to each propeller equipped motor $i \in \{1,2,3,4\}$ rotation speed, and $\omega_{\mathcal{M}_k}$ to the Magnus cylinder equipped motor $k \in \{r,l\}$.

3.2 Drone Forces:

- The forces applied to the system by the four propellers $i \in \{1,2,3,4\}$ are :

$$\boldsymbol{F}_{R_i}^m = C_T||\boldsymbol{w}^{\mathcal{R}_i\mathcal{D}}||^2\boldsymbol{d}_3 \tag{3.3}$$

with C_T generalized thrust coefficient and $\boldsymbol{w}^{\mathcal{R}_i\mathcal{D}}$ is the angular velocity vector of each rotor i such that,

$$\boldsymbol{w}^{\mathcal{R}_i\mathcal{D}} = w_{R_i}\boldsymbol{d}_3 \tag{3.4}$$

Therefore, the total thrust force exerted by the four propellers is

$$\boldsymbol{F}_D^m = \sum_i \boldsymbol{F}_{R_i}^m \tag{3.5}$$

- The aerodynamic forces due to its motion through the apparent wind speed. We consider here only the aerodynamic drag forces of the drone's body, which is computed as

$$\boldsymbol{F}_D^a = \frac{1}{2}\rho C_D||\boldsymbol{v}_a||^2\boldsymbol{S} \tag{3.6}$$

with C_D is the drone's drag coefficient and $\boldsymbol{S}$ is the drone's exposed surface vector. $\boldsymbol{v}_a$ is the apparent wind speed, considering $\boldsymbol{v}_w$ as the wind velocity vector, we get

$$\boldsymbol{v}_a = \boldsymbol{v}_w - \boldsymbol{v}_C^{\mathcal{I}} \tag{3.7}$$

3.3 Magnus Forces:

The aerodynamic characteristics of the Magnus cylinder are affected by various factors. The most important one that controls the Magnus effect-based wing is its spin ratio X, which is the ratio between the rotational speed of the Magnus wing and the apparent wind velocity $\boldsymbol{v}_a$, such that for each Magnus wing $k \in \{r, l\}$

$$X_k = \frac{R_{M_k} ||\boldsymbol{w}^{\mathcal{M}_k \mathcal{D}}||}{||\boldsymbol{v}_a||} \tag{3.8}$$

In this work, we chose to add endplates to the two Magnus cylinders. This can significantly enhance lift and improve the lift-to-drag ratio while maintaining a small aspect ratio $\Lambda = 5.1$. The endplate diameter was chosen to be twice that of the Magnus cylinder. The drag and lift coefficients dynamics are extracted from the wind tunnel tests gathered and analyzed in [12]. These forces can be derived as follows:

$$\begin{aligned} \boldsymbol{F}^D_{M_k} &= \frac{1}{2}\rho C_{D_k} S_{M_k} ||\boldsymbol{v}_{a_k}||^2 \boldsymbol{e}_{D_k} \\ \boldsymbol{F}^L_{M_k} &= \frac{1}{2}\rho C_{L_k} S_{M_k} ||\boldsymbol{v}_{a_k}||^2 \boldsymbol{e}_{L_k} \end{aligned} \tag{3.9}$$

such that S_{M_k} represents the projected surface area of each $k \in \{r, l\}$ Magnus cylinder and the aerodynamic drag and lift coefficient of the right and left Magnus cylinders are as follows:

$$\begin{cases} C_{D_k} := C_{D_k}(\boldsymbol{w}^{\mathcal{M}_k \mathcal{D}}, ||\boldsymbol{v}_{a_k}||) \\ C_{L_k} := C_{L_k}(\boldsymbol{w}^{\mathcal{M}_k \mathcal{D}}, ||\boldsymbol{v}_{a_k}||) \end{cases} \tag{3.10}$$

The apparent wind velocity experienced by right and left cylinders at their respective center of mass M_r and M_l respectively are:

$$\begin{aligned} \boldsymbol{v}_{a_r} &= \boldsymbol{v}_a + \frac{L_{M_r}}{2} r \boldsymbol{d}_1 \\ \boldsymbol{v}_{a_l} &= \boldsymbol{v}_a - \frac{L_{M_l}}{2} r \boldsymbol{d}_1 \end{aligned} \tag{3.11}$$

The directions of the drag and lift forces for each Magnus wing $i \in \{r, l\}$ are defined such that the drag force is in the direction of the apparent wind velocity and the lift force is orthogonal to the Magnus wing axis of rotation and the apparent wind velocity, then we deduce:

$$\begin{cases} \boldsymbol{e}_{D_k} = \frac{[\boldsymbol{v}_{a_k}]^{\mathcal{D}}}{||\boldsymbol{v}_{a_k}||} \ , \\ \boldsymbol{e}_{L_k} = \boldsymbol{m}_{k_2} \times \boldsymbol{e}_{D_k} \end{cases} \tag{3.12}$$

Hence, the total aerodynamic forces of each Magnus wing are read as follows:

$$\begin{cases} \boldsymbol{F}^a_{M_r} = \boldsymbol{F}^D_{M_r} + \boldsymbol{F}^L_{M_r} \\ \boldsymbol{F}^a_{M_l} = \boldsymbol{F}^D_{M_l} + \boldsymbol{F}^L_{M_l} \end{cases} \tag{3.13}$$

3.4 Total Forces:

We can deduce the total forces applied to the system, in inertial frame $\mathcal{I}$, based on (3.3)-(3.13) as follows:

$$\begin{aligned} \boldsymbol{F}_C &= \boldsymbol{R}^{\mathcal{D}\mathcal{I}} \boldsymbol{F}^m_D \\ \boldsymbol{F}_D &= \boldsymbol{R}^{\mathcal{D}\mathcal{I}} \boldsymbol{F}^a_D \\ \sum_k \boldsymbol{F}_{M_k} &= \boldsymbol{R}^{\mathcal{D}\mathcal{I}} (\boldsymbol{F}^a_{M_r} + \boldsymbol{F}^a_{M_l}) \end{aligned} \tag{3.14}$$

3.5 Drone torques:

- Spinning drone torque:
  The drone yaw torque is defined as follows,

  $$\boldsymbol{\Gamma}^y_D = \sum_i (C_Q ||\boldsymbol{w}^{\mathcal{R}_i \mathcal{D}}|| \boldsymbol{w}^{\mathcal{R}_i \mathcal{D}}) \tag{3.15}$$

  such that C_Q is the propeller's drag coefficient.

- Torque induced by the drone's motors thrust forces is computed as follows:

  $$\boldsymbol{\Gamma}^m_D = \sum_i (\boldsymbol{s}_{R_i C} \times \boldsymbol{F}^m_{R_i}) \tag{3.16}$$

  where $\boldsymbol{s}_{R_i C}$ for $i \in \{1, 2, 3, 4\}$ specifies the drone's geometry.

- Gyroscopic Effect drone torques:
  As the drone's rotors $\mathcal{R}_i$ for $i \in \{1, 2, 3, 4\}$ is spinning around $\boldsymbol{d}_3$, then if the system is rolling or pitching, a gyroscopic torque is resulted as follows:

  $$\boldsymbol{\Gamma}^g_D = I_r \sum_i (\boldsymbol{\omega}^{\mathcal{R}_i \mathcal{D}} \times \boldsymbol{w}^{\mathcal{D}\mathcal{I}}) \tag{3.17}$$

  with I_r as the rotor and propeller moment of inertia.

- Inertial rotation torque:

  $$\boldsymbol{\Gamma}^i_D = -I_r \sum_i (D^{\mathcal{D}} \boldsymbol{w}^{\mathcal{R}_i \mathcal{D}}) \tag{3.18}$$

3.6 Magnus torques:

- Spinning torque:
  The Magnus cylinder pitch torque is defined as follows,

  $$\boldsymbol{\Gamma}^p_M = \sum_k (C_{Q_k} ||\boldsymbol{w}^{\mathcal{M}_k \mathcal{D}}|| \boldsymbol{w}^{\mathcal{M}_k \mathcal{D}}) \tag{3.19}$$

  such that $C_{Q_k} = \frac{1}{2}\rho\pi C_f S_{M_k} R^3_{M_k}$ and C_f is the skin friction coefficient of cylinder surface [13].

- Magnus cylinder Aerodynamic torques: torques arise due to the difference between the lift and drag produced by each cylinder and are expressed as:

  $$\begin{cases} \boldsymbol{\Gamma}^a_{M_r} = \boldsymbol{s}_{M_r C} \times \boldsymbol{F}^a_{M_r} \\ \boldsymbol{\Gamma}^a_{M_l} = \boldsymbol{s}_{M_l C} \times \boldsymbol{F}^a_{M_l} \\ \boldsymbol{\Gamma}^a_M = \boldsymbol{\Gamma}^a_{M_r} + \boldsymbol{\Gamma}^a_{M_l} \end{cases} \tag{3.20}$$

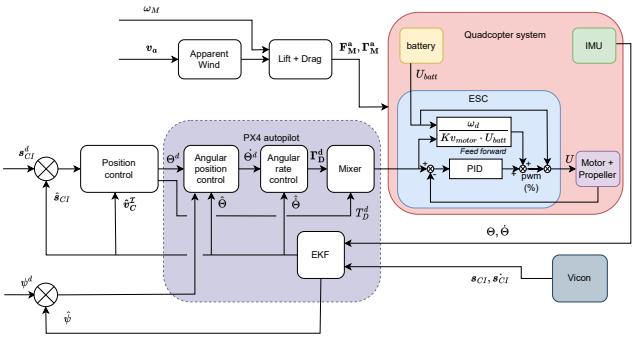

Figure 3: Magnus-based quadcopter control architecture

- Gyroscopic Effect and inertial Magnus torques: We can see from (2.5) that the last two terms represent, respectively, the gyroscopic and inertial rotation torques of the two Magnus cylinders such that

$$\begin{aligned} \boldsymbol{\Gamma}_M^g &= -\sum_k (\boldsymbol{\Omega}^{\mathcal{DI}} \boldsymbol{I}_{M_k}^{\mathcal{M}_k} \boldsymbol{w}^{\mathcal{M}_k \mathcal{D}}) \\ \boldsymbol{\Gamma}_M^i &= -\sum_k (\boldsymbol{I}_{M_k}^{\mathcal{M}_k} D^{\mathcal{D}} \boldsymbol{w}^{\mathcal{M}_k \mathcal{D}}) \end{aligned} \tag{3.21}$$

3.7 Total torques:

Torques from (3.21) could be included in torques exerted by Magnus cylinders, and thus the angular velocity dynamics (2.5) can be simplified,

$$\boldsymbol{J} D^{\mathcal{D}} \boldsymbol{w}^{\mathcal{DI}} = -\boldsymbol{\Omega}^{\mathcal{DI}} \boldsymbol{J} \boldsymbol{w}^{\mathcal{DI}} + \boldsymbol{\Gamma}_C + \boldsymbol{\Gamma}_D + \sum_k \boldsymbol{\Gamma}_{M_k} \tag{3.22}$$

Therefore, we can deduce the total torques applied to the system, in body frame $\mathcal{D}$, based on (3.15)-(3.21) as follows:

$$\begin{aligned} \boldsymbol{\Gamma}_C &= \boldsymbol{\Gamma}_D^y + \boldsymbol{\Gamma}_D^m \\ \boldsymbol{\Gamma}_D &= \boldsymbol{\Gamma}_D^g + \boldsymbol{\Gamma}_D^i \\ \sum_k \boldsymbol{\Gamma}_{M_k} &= \boldsymbol{\Gamma}_M^p + \boldsymbol{\Gamma}_M^a + \boldsymbol{\Gamma}_M^g + \boldsymbol{\Gamma}_M^i \end{aligned} \tag{3.23}$$

4 Control Strategy

In this section, we present the design of the overall control strategy. The control strategy is based on a simplified model of the system. This simplified model comes from a simplification of the complete nonlinear model, described in (2.3) and (3.22), in which aerodynamic effects, ground effect, and gyroscopic effects are neglected. This model is described as follows:

$$\begin{cases} \dot{\boldsymbol{s}}_{CI} &= \boldsymbol{v}_C^{\mathcal{I}} \\ m\dot{\boldsymbol{v}}_C^{\mathcal{I}} &= \boldsymbol{F}_C + \boldsymbol{P} \\ \dot{\boldsymbol{\Theta}} &= \boldsymbol{W}^{-1} \boldsymbol{w}^{\mathcal{DI}} \\ \boldsymbol{J}\dot{\boldsymbol{w}}^{\mathcal{DI}} &= -\boldsymbol{\Omega}^{\mathcal{DI}} \boldsymbol{J} \boldsymbol{w}^{\mathcal{DI}} + \boldsymbol{\Gamma}_C \end{cases} \tag{4.1}$$

4.1 Position and Velocity Loop:

The system's position and velocity can be controlled by $\boldsymbol{F}_C$. The latest is represented by its projections in the inertial frame $\mathcal{I}$: $F_{C_x}, F_{C_y}, F_{C_z}$ that controls x, y, z loops respectively. We have implemented the PID control strategy to compute these control forces for each loop $q \in \{x, y, z\}$, as follows:

$$F_{C_q} = m(k_{d_q}\dot{q} + k_{p_q} q + k_{i_q} \int e_q d\tau) \tag{4.2}$$

with e_q is the tracking error of each loop $q \in \{x, y, z\}$. The desired thrust force T_D^d and the desired Euler angles $\boldsymbol{\Theta}^d$ feed the inner loops. These are derived from (4.2) according to the kinematic transformation as follows:

$$\begin{cases} T_D^d &= m(F_{C_x} + g)/(c_\phi c_\theta) \\ \theta^d &= \text{atan2}((F_{C_x} c_\psi + F_{C_y} s_\psi), F_{C_z} + g), \\ \phi^d &= \text{atan2}(c_\theta((F_{C_x} s_\psi - F_{C_y} c_\psi), F_{C_z} + g) \end{cases} \tag{4.3}$$

4.2 Attitude and Angular Velocities Loops:

The simplified model in (4.1) gives a general view of the inner attitude and angular velocities control loops. On the one hand, the angular position represented by the Euler angles $\boldsymbol{\Theta}$ can be controlled by the angular velocities $\boldsymbol{w}^{\mathcal{DI}}$. On the other hand, the angular velocities $\boldsymbol{w}^{\mathcal{DI}}$ can be controlled by the controller torque $\boldsymbol{\Gamma}_C$. We use a PX4 onboard autopilot [14]. This autopilot manages the attitude and angular speed loops. The PX4 control structures for rate and attitude loops have been copied in the MATLAB/Simulink simulator based on in-flight tune control gains and control diagrams given by PX4.

4.3 PX4 Mixers

- PX4 Normalized Mixer: The hover compensation is applied to account for any variations in the drone's hover performance. The normalized desired total thrust force is computed as, $T_D^n = \frac{hc}{mg} T_D$ with hc is the hover compensation factor dependent on the specific drone and its configuration.

- PX4 Identified Mixer: It is based on a linear relationship between torque $\boldsymbol{\Gamma}_C$ and force T_D commands and the four rotors PWM signals setpoint. It is described as:

$$\begin{bmatrix} \boldsymbol{w}_{R_1} \\ \boldsymbol{w}_{R_2} \\ \boldsymbol{w}_{R_3} \\ \boldsymbol{w}_{R_4} \end{bmatrix} = \boldsymbol{M}_{PX4} \begin{bmatrix} \boldsymbol{\Gamma}_C \\ T_D^n \end{bmatrix} \tag{4.4}$$

5 Experimental setup

Our custom-built quadcopter flies on a Hollybro Pixhawk 4 flight controller running PX4 Autopilot. Offboard position control is performed on a ground station through ROS1. Communication between the UAV and the ground station is performed via Mavlink protocol through Wifi. To perform an indoor flight, as GPS (GNSS receiver) is not available, the Vicon motion capture system provides position measurement. The UAV is running on a 4S LiPo battery. All material is listed in Table 2 and diagrammed in Figure 4

Brushless motor speed control is performed with an ESC (Electronic Speed Controller). The ESC is meant to apply a fraction of the battery voltage to the motor. This fraction is given by a standard digital input (most generally PWM or Dshot signal). Thus, common motor control is performed in *open loop* concerning the desired rotation speed. In practice, air and dry friction cause the motor to run slower than expected. To achieve precise speed control and, thus, precise force control on each motor, we have implemented custom firmware into standard ARM32 processor-based ESCs, allowing *close loop* speed control. In our experimental setup, the input of the ESC is then a desired speed and not a percentage of battery voltage. In the ESC, speed control is performed through a standard PID regulation. Speed measurement is performed by monitoring the inversion of phase current due to the movement of rotor magnets. The ESC firmware that has been used is available at [1].

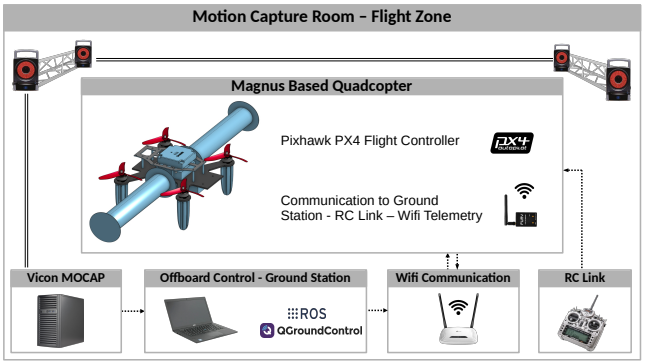

Figure 4: Gipsa-Lab experimental setup

6 Reliability Study

To study the reliability of our model, we propose a three-step approach to compare flight data to simulated ones. The propulsion model will be validated with a dedicated protocol detailed in Section 6.1. We will validate inner loops, inertia, and body dynamics on a position step scenario with no cylinders spinning. Finally, added gyroscopic effects will be assessed under a constant cylinder rotation speed scenario. Inertial effects will be shown in the inner attitude and rate loops by changing the rotational speed of the cylinders. Modeling the aerodynamics of the Magnus cylinders necessitates significant linear and rotational speed testing scenarios, which are not performed in this work. Lift and drag aerodynamics are not addressed in this work as they are well documented in the literature. We are then focusing on low linear speed scenarios. These torques and forces need significant linear speed and rotational speed. At this study stage, we based on the Magnus aerodynamic model already published as stated in Section 3.3. However, from a future perspective, these dynamics will be validated during external flights at higher speeds.

[1] https://github.com/gipsa-lab-uav/AM32-MultiRotor-ESC-firmware

Item	Description
Flight controller	Holybro Pixhawk 4 with PX4 v1.14 firmware
Battery	Bashing 4S 5000mAh
Radiocontroller	FrSky Taranis X9D
RC receiver	FrSky XM+
Motor	T-Motor F60proV 1750 Kv
Propeller	T-Motor T5147
Propeller ESC	HGLRC 4in1 Zeus 45A
Magnus ESC	HGLRC T-Rex 35A
Wifi Communication	ESP32 dev kit with serial/wifi bridge firmware
Motion capture system	12 Vicon T40s cameras, Tracker software

Table 2: Hardware setup

6.1 *Propulsion model validation*

The propulsion model, defined in Section 3.1 as a model of a single-phase motor combined with a 5-inch propeller, has been validated experimentally. As explained in Section 4.3, the PX4 autopilot performs a linear mix between the desired forces from the position controller and the desired motor speed fed to the ESC. However, as stated in Section 3.1, the generated force is not linear but proportional to the squared rotation velocity of the propeller.

In our control law, we work with a linear approximation of the thrust around the equilibrium point of hover flight for a given flight mass. To experimentally validate the propeller model used in (3.3), we maintained the UAV in a hoover flight with a position control based on the linear approximation of the thrust. Then, every 10 seconds, an additional mass of 60 grams is added to the UAV. We monitored desired motor speeds [rad.s-1] and desired Thrust [N]. Figure 5 shows the experimental validation of the propulsion model and of its linear approximation around the flight mass equilibrium point: the estimation of the thrust as proportional to the sum of squared velocities of propellers matches the actual mass of the UAV, whereas its linear approximation used for control fits with the actual value around the real flight mass. The lift coefficient C_T has been calculated from desired motor speeds

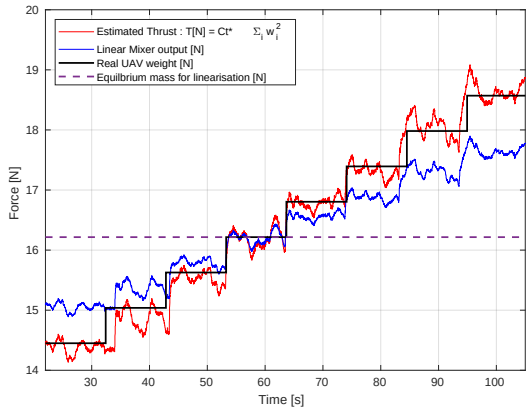

Figure 5: Experimental Thrust model validation

and real UAV weight during the protocol.

6.2 *Dynamical Model without Magnus rotation*

Figures 6, 7, 8 and 9 show comparison between flight data and simulator data of all nested loops dynamics over the same 3D position steps scenario and no cylinder rotation. A yaw step is performed at $t = 110s$. Even if the noise level over the angular rates and attitude loops, as shown in Figures 6 and 7, is under-estimated in the simulator, the main dynamics remain correctly predicted. These noises are mainly due to unmodelled vibrations on the UAV frame and unmodelled aerodynamic disturbances in an indoor environment (wind turbulence).

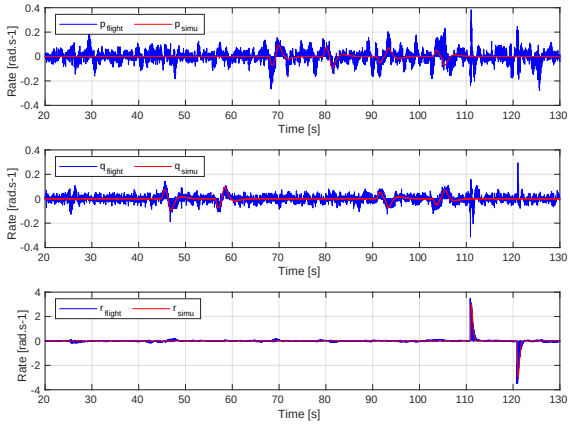

Figure 6: Angular velocities response in case of no Magnus rotation

6.3 *Magnus cylinder induced disturbances*

- To highlight the gyroscopic effects due to cylinders rotation, let's focus on the effect of a yaw step in hovering flight at constant cylinder speed $\omega_{\mathcal{M}_r} = \omega_{\mathcal{M}_l} = 7200$rpm over the angular rate p, as shown in Figure 10.
- To highlight the effects of inertia due to cylinder rotation, let's vary cylinder speed in hovering flight between

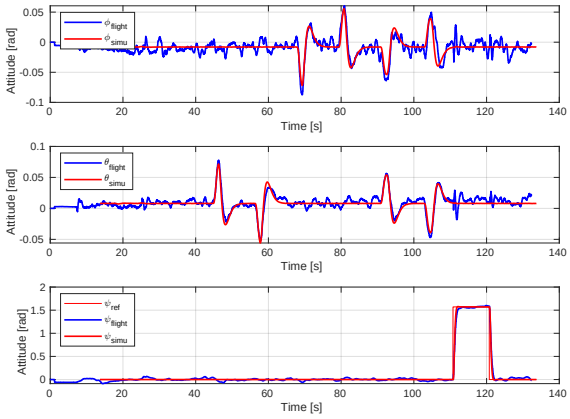

Figure 7: Euler angles response in case of no Magnus rotation

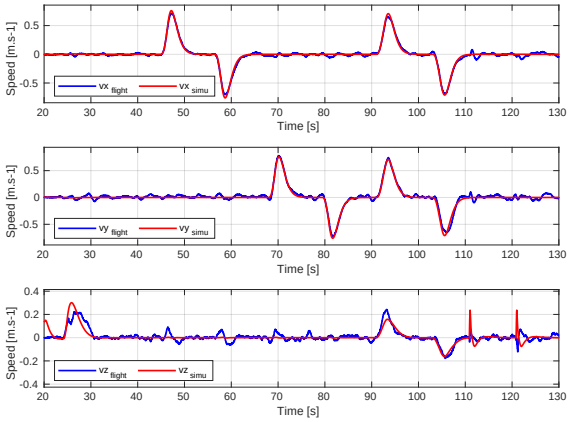

Figure 8: Linear velocities response in case of no Magnus rotation

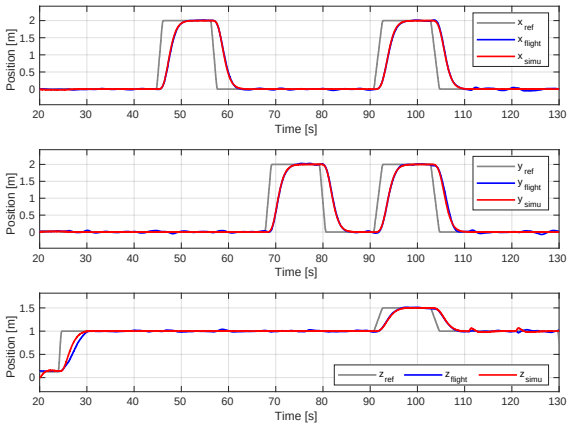

Figure 9: Positions response in case of no Magnus rotation

$\omega_{\mathcal{M}_r} = \omega_{\mathcal{M}_l} = 5100$ rpm (rotations per minutes) and $\omega_{\mathcal{M}_r} = \omega_{\mathcal{M}_l} = 11400$ rpm. We simulate and monitor an added inertial torque among the body $\boldsymbol{d}_2$ axis as shown in Figure 11, on the rate and attitude loops. The acceleration of the cylinders is shown at the top of the figure.

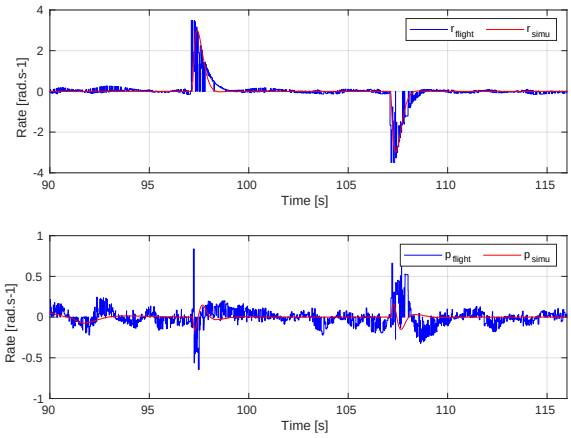

Figure 10: Magnus gyroscopic effect on p rate

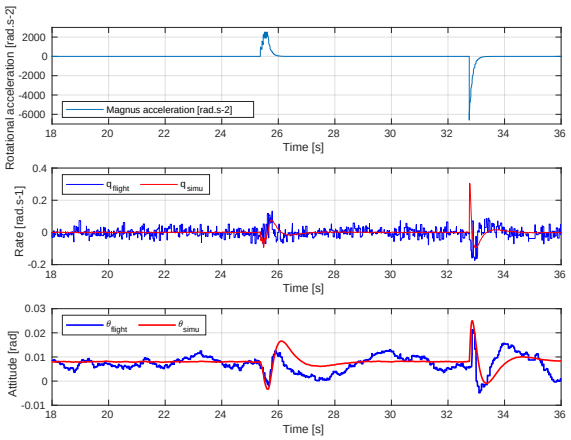

Figure 11: Magnus inertial effects among body $\boldsymbol{d}_2$ axis

The Magnus rotor friction torque is estimated to be $1.8e-3$ Nm for maximal rotation speed at 11400 rpm, which is negligible regarding other torques acting on the system.

7 Conclusion

This paper presented the design and experimental validation of a 6-DoF simulator for a Magnus-based quadcopter system. This simulator was validated based on flight experimental tests in an indoor environment and loop-by-loop validation. The results demonstrate that the simulator accurately captures the central dynamics of the system. Its reliability and compatibility with experimental data make it a tool for researchers and engineers to optimize Magnus-based quadcopter systems' design and control strategies. The findings contribute to Magnus-based quadcopters and enable their use in various industries, paving the way for efficient and capable unmanned aerial vehicles. For future work, it is recommended to incorporate more sensors and an Extended Kalman Filter and validate the simulator based on outdoor experiments with higher speed maneuvers.

Acknowledgements

This work has been partially supported by ROBOTEX 2.0 (Grants ROBOTEX ANR-10-EQPX-44-01 and TIRREX ANR-21-ESRE-0015), funded by the French program Investissements d'avenir.

References

[1] Giuseppe Silano, Jan Bednar, Tiago Nascimento, Jesus Capitan, Martin Saska, and Anibal Ollero. A multi-layer software architecture for aerial cognitive multi-robot systems in power line inspection tasks. In *ICUAS*, 2021.

[2] Weibin Gu, Dewen Hu, Liang Cheng, Yabing Cao, Alessandro Rizzo, and Kimon P. Valavanis. Autonomous wind turbine inspection using a quadrotor. In *ICUAS*, 2020.

[3] Arturo Torres-González, Jesús Capitán, Rita Cunha, Anibal Ollero, and Ioannis Mademlis. A multidrone approach for autonomous cinematography planning. In *ROBOT 2017: Third Iberian Robotics Conference*.

[4] David Schneider. The delivery drones are coming. *IEEE Spectrum*, 57(1):28–29, January 2020.

[5] Suseong Kim, Seungwon Choi, and H. Jin Kim. Aerial manipulation using a quadrotor with a two DOF robotic arm. In *2013 IEEE/RSJ*.

[6] Jost Seifert. A review of the magnus effect in aeronautics. *Progress in Aerospace Sciences*, 55:17–45, 2012.

[7] Yashank Gupta, Jonathan Dumon, and Ahmad Hably. Modeling and control of a magnus effect-based airborne wind energy system in crosswind maneuvers. *IFAC-PapersOnLine*, 50(1):13878–13885, 2017.

[8] Zakeye Azaki, Jonathan Dumon, Nacim Meslem, Ahmad Hably, and Pierre Susbielle. Modelling and control of a tethered drone for an awe application. In *ICCAD 2022*, 2022.

[9] Lorenzo Fagiano, Manfred Quack, Florian Bauer, Lode Carnel, and Espen Oland. Autonomous airborne wind energy systems: accomplishments and challenges. *Annual Review of Control, Robotics, and Autonomous Systems*, 5:603–631, 2022.

[10] Zakeye Azaki, Jonathan Dumon, Nacim Meslem, and Ahmad Hably. Sliding mode control of tethered drone: Take-off and landing under turbulent wind conditions. In *ICUAS*, 2023.

[11] P. H. Zipfel. *Modeling and Simulation of Aerospace Vehicle Dynamics*. American Institute of Aeronautics and Astronautics, Inc., 3rd edition, 2014.

[12] C. Badalamenti, , and S. Prince. Effects of endplates on a rotating cylinder in crossflow. *Applied Aerodynamin Conference*, 2008.

[13] C. Badalamenti. On the application of rotating cylinders to micro air vehicle. *Unpublished Doctoral thesis, City University London*, 2010.

[14] Dario Brescianini, Markus Hehn, and Raffaello D'Andrea. Nonlinear quadrocopter attitude control: Technical report. Technical report, 2013.